Impact of oxygen doping and oxidation state of iron on the electronic and magnetic properties of $BaFeO_{3-\delta}$

I. V. Maznichenko,[1,*] S. Ostanin,[2] L. V. Bekenov,[3] V. N. Antonov,[2,3] I. Mertig,[1,2] and A. Ernst[2]

[1]*Institut für Physik, Martin-Luther-Universität Halle-Wittenberg, D-06099 Halle, Germany*

[2]*Max-Planck-Institut für Mikrostrukturphysik, Weinberg 2, D-06120 Halle, Germany*

[3]*Institute of Metal Physics, Vernadsky Street, 03142 Kiev, Ukraine*

(Received 28 May 2015; revised manuscript received 17 December 2015; published 15 January 2016)

We studied the structural, electronic, and magnetic properties of a cubic perovskite $BaFeO_{3-\delta}$ ($0 \leqslant \delta \leqslant 0.5$) within the density-functional theory using a generalized gradient approximation (GGA) and a GGA + U method. According to our calculations, $BaFeO_3$ in its stoichiometric cubic structure should be half-metallic and strongly ferromagnetic, with an extremely high Curie temperature (T_C) of 700–900 K. However, such an estimate of T_C disagrees with all available experiments, which report that T_C of the $BaFeO_3$ and undoped $BaFeO_{3-\delta}$ films varies between 111 and 235 K, or, alternatively, that no ferromagnetic order was detected there. Fitting the calculated x-ray magnetic circular dichroism spectra to the experimental features seen for $BaFeO_3$, we concluded that good agreement can be obtained when oxygen vacancies are included in our model. Thus, the relatively low T_C measured in $BaFeO_3$ can be explained by oxygen vacancies intrinsically present in the material. Since iron species near the O vacancy change their oxidation state from 4+ to 3+, the interaction between Fe^{4+} and Fe^{3+}, which is antiferromagnetic, weakens the effective magnetic interaction in the system, which is predominantly ferromagnetic. With increasing δ in $BaFeO_{3-\delta}$, its T_C decreases down to the critical value when the magnetic order becomes antiferromagnetic. Our calculations of the electronic structure of $BaFeO_{3-\delta}$ illustrate how the ferromagnetism originates and also how one can keep this cubic perovskite robustly ferromagnetic far above room temperature.

DOI: 10.1103/PhysRevB.93.024411

I. INTRODUCTION

A multiferroic tunnel junction, in which a robust ferroelectric barrier, such as $PbTiO_3$ or $BaTiO_3$, is grown epitaxially between two ferromagnetic electrodes, allows us to tune the spin transport by switching the magnetization of an electrode. Additionally, the barrier polarization reversal can change the interfacial magnetoelectric coupling, and thus a four-state tunneling resistance can be detected [1,2]. As for the upper electrode, the Fe and Co films can easily be grown on the TiO_2-terminated polar perovskites [3], while the best bottom-electrode material, which can be used here as the substrate, must satisfy the following conditions: (i) its structure should be in a good lattice match with the ferroelectrics, and (ii) the electrode material should be robustly ferromagnetic with a relatively high Curie temperature (T_C). A very good choice would be a magnetic perovskite since a ferroelectric can be well grown on such substrates. In particular, perovskites ABO_3 with a magnetic cation on site B are well known to be compatible with ferroelectrics [4]. Recently, Pantel *et al.* [5] demonstrated the four-state tunneling resistance effect using the 3.2-nm-thick perovskite barrier $PbZr_{0.2}Ti_{0.8}O_3$ (001) grown on ferromagnetic La(Sr)MnO_3 (LSMO).

One of the possible candidates for the substrate in a multiferroic tunnel junction seems to be $BaFeO_3$ (BFO). Although bulk BFO is hexagonal, the perovskite phase can be stabilized in epitaxial films. X-ray diffraction studies show that thin BFO films grown on $SrTiO_3$(001) adopt the cubic perovskite structure with a lattice parameter of 3.97 Å [6,7]. For $BaFeO_{3-\delta}$ films, a larger lattice parameter of 4.07 Å has been measured [8]. Regarding the observed magnetic properties of the cubic BFO, such as the Fe magnetic moment, magnetic ordering, and T_C, the reports seem contradictory. Callender *et al.* [9] reported that a pseudocubic BFO is robustly ferromagnetic (FM) with $T_C = 235$ K. Instead, the oxygen-deficient $BaFeO_{3-\delta}$ films exhibit antiferromagnetism (AFM) at room temperature, while a weakly ferromagnetic behavior extends above 390 K [8]. For thick BFO films, Chakraverty *et al.* [6] reported $T_C = 115$ K and a saturation magnetization of $3.2\mu_B$/f.u., which both remain stable as a function of film thickness, with no signature of the spin spiral structure up to 300 nm.

In the case of completely oxidized stoichiometric cubic BFO, the oxidation state of iron is 4+, which leads to the twofold orbitally degenerate configuration $t_{2g}^3 e_g^1$. In polyatomic molecules, the half-occupied e_g level has to split according to Jahn and Teller [10]. In solids the effect must be cooperative. However, for $AFeO_3$ (A = Ca,Sr,Ba) this behavior, known as the cooperative Jahn-Teller distortion, was not reported so far. Instead, it occurs in antiferromagnetic $LaMnO_3$ where up to 750 K the e_g splitting opens the band gap [11–13]. On the other hand, the Fe oxidation state in oxides is so unstable that the presence of the degenerated e_g level is not required. For instance, in metallic $CaFeO_3$ a charge disproportion is observed: $2Fe^{4+} \rightarrow Fe^{(4-\tau)+} + Fe^{(4+\tau)+}$, where $0 < \tau \leqslant 1$ [14]. Thus, the issue of mixed valency might be very important in the case of BFO.

Several theoretical studies of magnetic BFO have recently been made from first principles. For the FM order and experimental lattice parameter of the cubic BFO, the calculated magnetic moment varies between $3.0\mu_B$ and $3.4\mu_B$ per f.u. [15,16], depending on the model approximation used to treat the exchange-correlation effects. According to the

*igor.maznichenko@physik.uni-halle.de

ab initio investigation by Ribeiro *et al.* [17], the FM solution in the stoichiometric BFO is energetically favored against the possible AFM configurations, and the FM moment is about $3.6\mu_B$. A helical magnetic ordering in BFO, which is usually discussed in the context of $SrFeO_3$ and $CaFeO_3$ [18], has been investigated from first principles by Li *et al.* [19,20]. The authors anticipate that a G-type helical solution can be fixed, keeping the reduced volume and, simultaneously, using the Hubbard parametrization, which treats electronic correlations beyond the standard local-density approximation. No theoretical estimations of T_C were performed so far.

As was already mentioned above, the Fe atoms in BFO can have various oxidation states. The origin of this distinction in real materials can be related, for instance, to a particular sample preparation procedure, which can explain the large discrepancy in the results of various experiments. In this work, we investigated from first principles the impact of Fe oxidation states on the structural, magnetic, optical, and electronic properties of chemically perfect BFO and $BaFeO_{3-\delta}$ ($\delta > 0$) with vacancies. To obtain a realistic structure of BFO, we simulated XAS and XMCS spectra from first principles for various structural and oxidation scenarios, and we compared them with available experimental results. Since XAS and XMCD spectroscopy are very sensitive to the fine details of the crystalline, electronic, and magnetic structures, this approach can be very efficient for oxides, which have usually a nontrivial complex chemical composition containing defects, vacancies, and various oxidation states of cations. Another complication is the presence of strongly localized $3d$ electrons of Fe, which in many cases cannot be adequately described within conventional density-functional approximations such as the LDA or the GGA. Here again, we used a direct comparison of theoretically obtained XAS and XMCD spectra with experiment to choose an appropriate value of the Hubbard parameter U within the applied GGA + U method to treat efficiently strongly localized $3d$ Fe states.

The paper is organized as follows. In Sec. II, we provide the essential details of our methods and calculations. In Sec. III, we present the results and discuss the structural, electronic, optical, and magnetic properties of the BFO. Finally, our summary and conclusions are drawn.

II. DETAILS OF CALCULATIONS

Our calculations of BFO, undoped $BaFeO_{3-\delta}$, and nominally overdoped BFO were performed using a first-principles Green's-function method [21,22] based on multiple-scattering within the density-functional theory in a generalized-gradient approximation (GGA) to the exchange-correlation potential [23]. We used a full charge-density treatment to take into account the possible nonsphericity of the crystal potential and the charge density. The maximal angular momentum used was $l_{\max} = 3$ and the integrals over the Brillouin zone were performed using the $16 \times 16 \times 16$ k-point mesh.

The Fe oxidation state was modeled using a self-interaction correction (SIC) method [24] as it is implemented within the multiple-scattering theory [21]. In this case, an oxidation state can be defined by the number of valence electrons as

$$N_{\text{val}} = Z - (N_{\text{core}} + N_{\text{SIC}}), \tag{1}$$

where Z is the total number of electrons of an isolated atom, N_{core} is the number of electrons occupying the deep energy levels and treated as the core electrons, and N_{SIC} is the number of SIC corrected $3d$ electrons.

Since the SIC approach is designed only for ground-state properties [24], we used a GGA + U method [25] to take into account electronic correlation effects in calculations of exchange parameters. The latter were estimated within the magnetic force theorem [26]. The critical temperature and the magnetic ordering were obtained within the Heisenberg model

$$H = -\sum_{i,j} J_{ij}\, \mathbf{e}_i \cdot \mathbf{e}_j, \tag{2}$$

where i and j label the magnetic atoms, and $\mathbf{e}_i$ is a unit vector in the direction of the magnetic moment of the i th atom. The critical temperatures were estimated using both the mean-field approximation (MFA) and random-phase approximation (RPA) [27]. Both approaches were successfully applied to many magnetically ordered oxides, including magnetic perovskites [28,29].

Disorder effects in our study were simulated within the coherent-potential approximation (CPA) [30–32]. The intrinsic oxygen vacancies in $BaFeO_{3-\delta}$ were modeled within the same CPA scheme, which implies randomly distributed vacancies over all oxygen sites. Regarding the Ba and Fe vacancies, in the literature, such cation-deficient perovskites are formally denoted as $BaFeO_{3+\delta}$, although the bulk perovskite structures are unable to accommodate interstitial oxygen.

The calculations of the XAS and XMCD were performed using the spin-polarized fully relativistic linear-muffin-tin-orbital (LMTO) method [33,34] for the experimentally observed lattice constants. More details for the XAS and XMCD simulations are described in our previous papers [35–37]. For these calculations, disorder effects were simulated using the supercell approach. We used a $2 \times 2 \times 4$ cell, which allows us to model an environment with neighboring Fe atoms of different valencies and an oxygen vacancy. The same supercell was used for calculations of exchange parameters to simulate short-range effect in the presence of an oxygen vacancy. The structural optimization of the supercell that contains oxygen vacancy was calculated using the Vienna *Ab initio* Simulation Package (VASP) [38] within the generalized-gradient approximation to the exchange-correlation potential. The electron-ion interactions were described by projector-augmented wave pseudopotentials, and the electronic wave functions were represented by plane waves with a cutoff energy of 500 eV. Ionic relaxation was performed using the Γ-centered $4 \times 4 \times 4$ k-point Monkhorst-Pack mesh and the conjugate-gradient algorithm until the Hellmann-Feynman forces became less than 10^{-3} eV/Å, which yielded reliable results for the atomic positions. The utilization of the Hubbard-U parametrization applied on the Fe d orbitals changes the relaxed atomic positions insignificantly.

III. RESULTS

A. Crystalline structure of $BaFeO_3$

The ground-state phase of BFO is hexagonal with the space-group symmetry $P12_1/c1$ [39]. However, a cubic FM

phase can be stabilized in thin films at room temperature by anharmonic contributions to the free energy and/or the effects of epitaxial strain. In the cubic BFO phase, the equilibrium lattice parameter is significantly underestimated within the LDA (3.86 Å) as compared to the experimental value of 3.97 Å, while the use of the GGA results in $a = 3.963$ Å. For the latter we found that the FM ordering is strongly favored by 110 meV/f.u. with respect to the G-type AFM configuration. Thus, the crystalline structure of the cubic BFO can be adequately described using the conventional GGA functional. Further, we focus our study on the electronic, optic, and magnetic properties of the cubic BFO phase (see Fig. 1, inset).

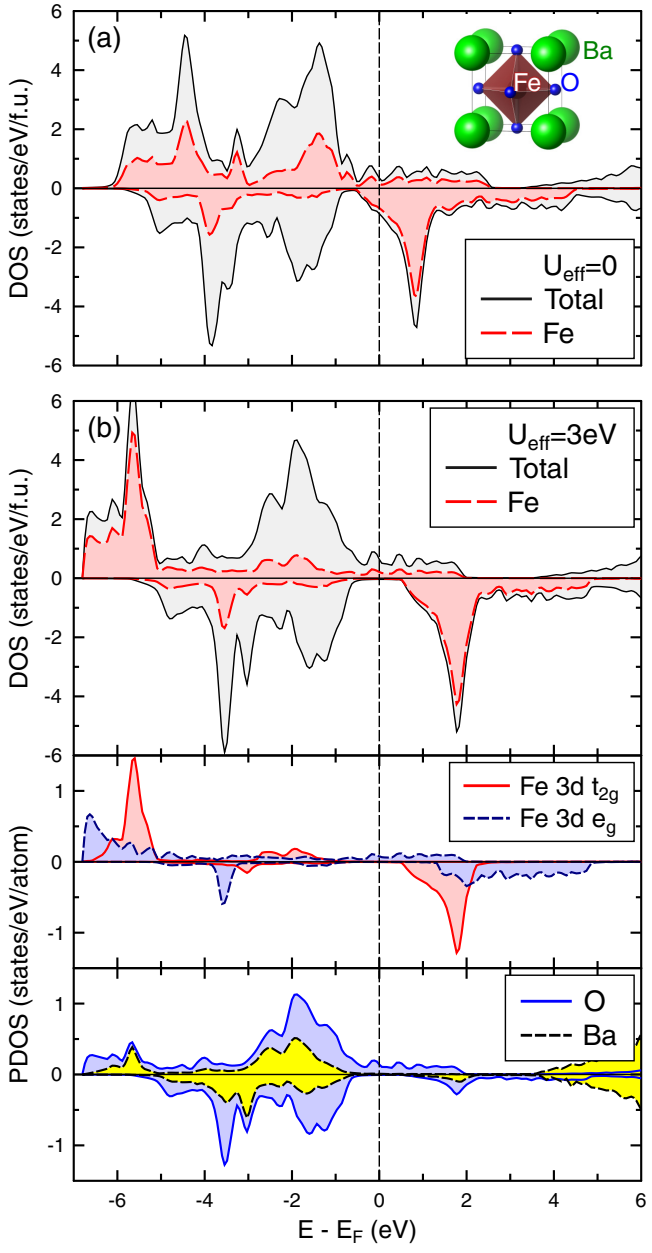

FIG. 1. The total and site-projected DOS of cubic BFO calculated within the GGA (a) and within the GGA + U method with $U_{\text{eff}} = 3$ eV. The positive (negative) DOS values denote the majority (minority) spin states. Inset: crystalline structure of the cubic $BaFeO_3$.

B. Electronic and magnetic structure of $BaFeO_3$

1. GGA approach

Since we found the GGA to be an appropriate functional in describing the crystalline structure of the cubic BFO, we applied the method for further studies of its electronic and magnetic properties. Within the GGA, the spin-polarized density of states (DOS) of BFO exhibits a metallic behavior in the two spin channels, as is shown in Fig. 1(a). This agrees with the experimental findings of Callender *et al.* [9], who observed the ferromagnetic ordering and conductance in BFO films, annealed in an oxygen atmosphere. The iron atoms appear to have the oxidation state of 2+. Therefore, the t_{2g} and e_g states are mostly occupied in the majority spin channel (4.5 electrons) and only partially occupied (1.5 electrons) in the minority spin channel. The 3d electrons of iron experience strong hybridization with the p states of oxygen, and they are widely spread over the whole valence-band region. The total magnetic moment, calculated within the GGA, is $3.55\mu_B$ per f.u., which includes the ferromagnetically induced O moments of about $0.15\mu_B$.

The exchange interaction between Fe atoms is large and positive within the GGA: 20.5 and 2 meV between the nearest and the next nearest neighbors, respectively. The estimated Curie temperature is about 1000 K in the mean-field approximation (700 K in the random-phase approximation). It should be mentioned here that the RPA provides usually a reasonable critical temperature, while the MFA represents an average exchange interaction and overestimates T_C by 30–40 % [40].

Thus, the Curie temperature, calculated in the cubic BFO using the GGA method, is several times larger than the experimental values (100–400 K). The reason is that the system is metallic within this approach and, therefore, the double exchange interaction via the oxygens and the band ferromagnetism dominates over the other exchange mechanisms, which can reduce the magnetic interaction or change its sign. Therefore, the electronic correlations, which can be substantial in oxides, must be taken into account using a more appropriate method.

2. GGA + U approach

At the next step, we chose the GGA + U approximation, which provides a more adequate description of oxide materials than the conventional LDA or GGA approaches [41]. Since we could not estimate the value of U from first principles, we used it as a parameter tracing the change of the electronic and magnetic properties with the value of U. In our simulations, we applied the Hubbard-U corrections on Fe 3d states and varied the value of $U_{\text{eff}} = U - J$ between 0 (here, GGA) and 9 eV. As expected, the occupied (unoccupied) 3d Fe states are shifted down (up) in energy by the value of $U_{\text{eff}}/2$ that opens the gap in the minority spin channel for $U_{\text{eff}} \geqslant 2$ eV [see the DOS in Fig. 1(b) with $U_{\text{eff}} = 3$ eV]. The size of the spin band gap depends strongly on the U_{eff} value.

In Fig. 2, we show the total and all site-projected magnetic moments, which are plotted as a function of $0 \leqslant U_{\text{eff}} \leqslant 9$. The local magnetic moment of iron increases from $3\mu_B$ to $4.18\mu_B$ within the given range of U_{eff} values, while the induced magnetic moment of oxygen decreases from $0.18\mu_B$

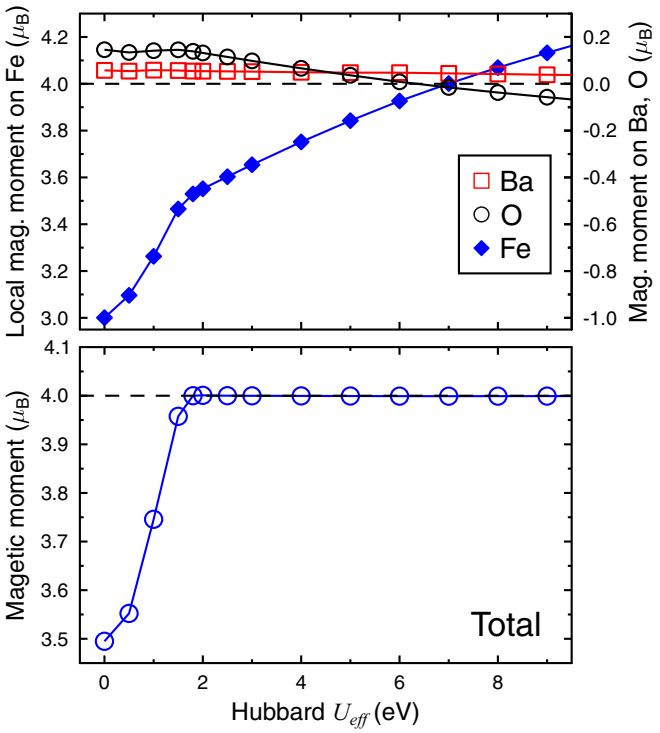

FIG. 2. The total and site-projected magnetic moments of cubic BFO calculated as a function of U. Here, $U_{\text{eff}} = 0$ means the use of the GGA.

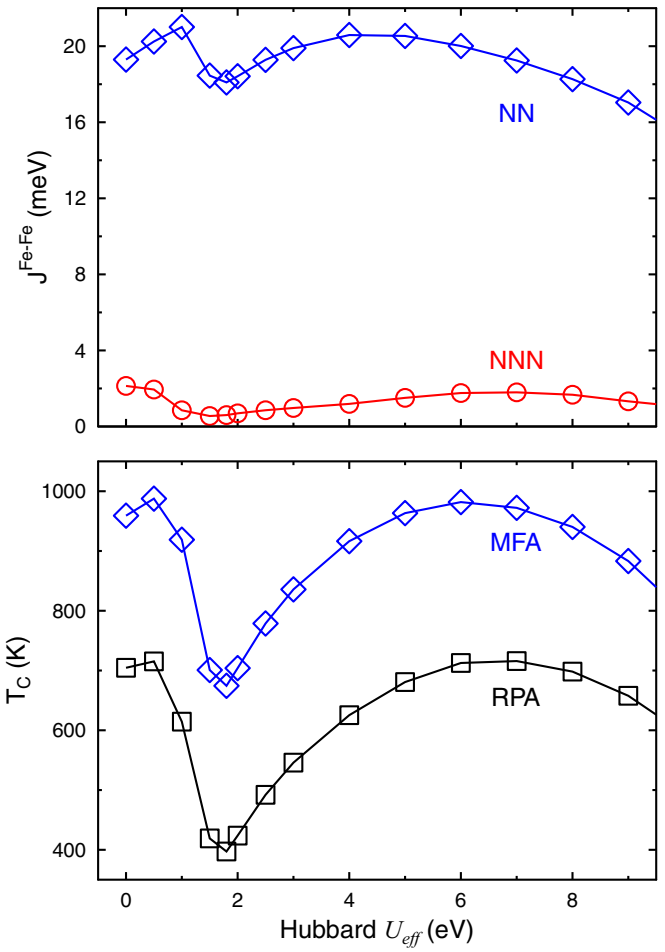

FIG. 3. Exchange interactions (upper panel) and the Curie temperature (lower panel) of the cubic BFO calculated as a function of the Hubbard parameter U_{eff} applied on the Fe $3d$ orbitals.

to $-0.08\mu_B$ systematically with the increase of U_{eff}. The magnetic moment induced on Ba is $\approx 0.05\mu_B$ and its small value changes marginally on the model variations of U. For $U_{\text{eff}} \geqslant 2$ eV, the total moment is integer ($4\mu_B$/f.u), which reflects the half-metallicity of the BFO. This is larger than the experimental values of 3.2–3.5μ_B/f.u., reported previously in Refs. [6,7].

Next, we calculated the exchange interaction as a function of U_{eff}. This test shows mainly how the exchange constants depend on the extend of a $3d$ electronic wave function. In a simple view, the exchange constants represent the overlap integrals between the electronic wave functions. The applied GGA + U method reduces the extent of the corrected wave function with the increase of the U value tuning by the corresponding overlap integrals.

The results are presented in Fig. 3. Since BFO remains metallic within this approximation, we can classify the main magnetic interaction as a double exchange. The consequence of the strong ferromagnetic coupling is the largely overestimated T_C compared to the measured values. Applying the GGA + U method slightly reduces the exchange interaction, mainly due to the reduction of the overlap between the Fe and oxygen states, but the Curie temperature is still too high in the whole range of U_{eff}. The dependence of T_C on U_{eff} is nontrivial. First, T_C reduces with the increase of U_{eff}, since the Fe $3d$ states are getting localized and their overlap with sp states of oxygen decreases. At $U_{\text{eff}} = 2$ eV, a band gap forms in the minority spin channel, and the $J^{\text{Fe-Fe}}$ rise up with the increase of U_{eff}. Therewith, the exchange interaction between the nearest neighbors gets larger only until $U_{\text{eff}} \approx 4$ eV and then it decreases, while the next-nearest-neighbor interaction continues to increase until $U_{\text{eff}} \approx 6$ eV. As a result, the Curie temperature reaches up to 700 K within the RPA for $U_{\text{eff}} \approx 6$ eV and then starts to decrease. According to our estimations, the Curie temperature agrees with experimental values only for $U_{\text{eff}} > 15$ eV, which are nonphysical for this compound. Thus, considering only electronic correlation effects does not explain the magnetic properties of BFO. This fact motivated us to improve the model of BFO and make further calculations.

C. Simulation of XMCD spectra

In complex transition-metal oxides, the XAS and XMCD spectra at the $L_{2,3}$ absorption edges can be used as fingerprints of the ground state. Since the XAS and XMCD spectra are sensitive to the local environment and the electronic structure, one can try to fit the experimental results by theoretical simulations probing various parameters of calculations. In our study, we simulated the XAS and XMCD spectra varying the crystal structure, the chemical composition, the value of U_{eff} for electronic correlation effects, and the magnetic order searching for an optimal agreement with available experiments.

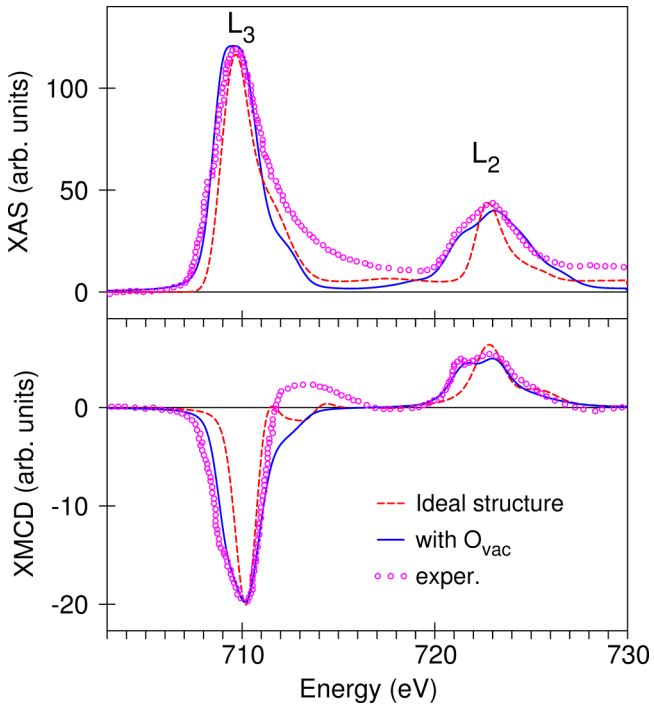

FIG. 4. Comparison between the experimental [43] x-ray absorption (upper panel) and x-ray magnetic circular dichroism (lower panel) at the Fe $L_{2,3}$ edges of $BaFeO_3$ and the spectra calculated in the GGA + U approximation ($U_{\text{eff}} = 3$ eV) (black solid lines). The red dashed line shows the spectra for the ideal crystal structure, while the dotted blue line presents the theoretical spectra with an oxygen vacancy.

In our study, we accounted for core-hole effects in the final state on the shape of the XAS and XMCD spectra. When a $3p$ core electron (in the $L_{2,3}$ XAS) is photoexcited to an unoccupied $3d$ state, the charge distribution changes to account for the created hole. Using a $2 \times 2 \times 4$ supercell, we created a hole in the Fe $2p_{1/2}$ ($2p_{3/2}$) shell in one of 16 Fe atoms of the supercell, and we calculated self-consistently the Fe L_2 (L_3) and O K XAS. In the case of XAS at the Fe $L_{2,3}$ edges, we found only a minor influence of the core-hole effects. This can be explained by the fact that the Fe $2p$ states are less localized as, for example, the $4f$ states in rare earths [42], and therefore they have a smaller amplitude inside the atomic sphere and thus are less subject to the core-hole potential. At the same time, the final-state interaction slightly improves the agreement between theory and experiment at O K XAS and XMCD spectra.

Figure 4 displays the experimentally measured [43] and theoretically calculated Fe $L_{2,3}$ XAS (upper panel) and XMCD (lower panel) spectra of cubic $BaFeO_3$. The L_3 XAS spectrum exhibits a weak lower-energy shoulder at around 708 eV together with a high-energy shoulder at 713 eV. The L_2 XAS spectrum exhibits a lower-energy peak at around 721 eV. The Fe L_3 XMCD spectrum consists of a major negative peak at 710 eV with a low-energy shoulder and an additional positive peak at 713 eV. The Fe L_2 XMCD spectrum has a double-peak structure.

First, we found that the best agreement with experiments was achieved for $U_{\text{eff}} = 3$ eV. This value of U_{eff} is used later for all our calculations if it is not mentioned specifically. However, the experimental results could not be explained only by taking into account strong correlation effects. For the ideal cubic BFO structure, our simulations of the XAS and XMCD spectra provide an x-ray-absorption intensity in the Fe L_3 only at the major peak and high-energy shoulder, while the low-energy peaks at the L_3 and L_2 edges are not reproduced (red dashed curve in Fig. 4). The calculation fails to reproduce the low-energy shoulder of the XMCD major negative peak at 709 eV in the L_3 XMCD spectrum. Also, the simulations for the ideal cubic BFO phase provide only a high-energy peak structure in the L_2 XMCD spectrum, whereas the experimental measurements exhibit a double-peak structure.

The correct explanation of the experimental XAS and XMCD spectra is only possible by taking into account crystal imperfections, namely oxygen vacancy. To investigate the influence of oxygen deficiency on the XAS and XMCD spectra, we created an oxygen vacancy in a $2 \times 2 \times 4$ supercell in the first neighborhood of the second Fe atom. We found that the presence of the oxygen vacancy decreases the valency of the nearest Fe ion from 4+ to 3+ (see the corresponding discussion below). The x-ray absorption from the Fe atoms with the oxygen vacancy in close vicinity (dotted blue line in Fig. 4) contributes to the low-energy peaks in the L_2 absorption and XMCD spectra. The oxygen vacancy also explains the existence of the low-energy shoulder in the Fe L_3 XMCD spectrum at 709 eV.

The same conclusion can be drawn from the interpretation of the XAS and XMCD spectra at the O K edge. Figure 5 shows the experimentally measured x-ray absorption and XMCD spectra [43] (open circles) at the O K edge in $BaFeO_3$ together with theoretically calculated spectra for the ideal crystal structure of $BaFeO_3$ (red dashed curves) and the structure with oxygen vacancy (dotted blue curves). The calculations for the ideal structure are not able to describe the high-energy shoulder of the major negative XMCD peak at 531 eV, which is due to the oxygen vacancy. We can conclude that the explanation of the experimental spectra at both the Fe $L_{2,3}$ and O K edges demands the presence of crystal imperfections in $BaFeO_3$.

D. Fe valency and oxygen vacancies in $BaFeO_{3-\delta}$

Summarizing our XAS and XMCD simulations, a real BFO in the cubic phase contains oxygen vacancies. The amount of vacancies depends definitely on the crystal growth and other experimental conditions. The oxygen vacancies affect strongly the valency of Fe atoms and the electronic structure of the whole sample. In this subsection, we discuss the vacancy formation in cubic BFO and its impact on the electronic and magnetic properties of this system.

To understand the vacancy formation, we performed first-principles studies of the Fe oxidation states in the cubic $BaFeO_3$ using a self-interaction method, as was described in Sec. II. The Fe oxidation state varies in different compounds from 2+ to 4+. For a completely oxidized BFO, one can expect a high valency, Fe^{4+}. The total energy study of the oxidation state and further comparison between BFO and $BaFeO_{3-\delta}$ can provide us with some hints concerning the electronic properties and the preferable magnetic order in BFO. The Goodenough-Kanamori rules of the 180° superexchange suggest that the

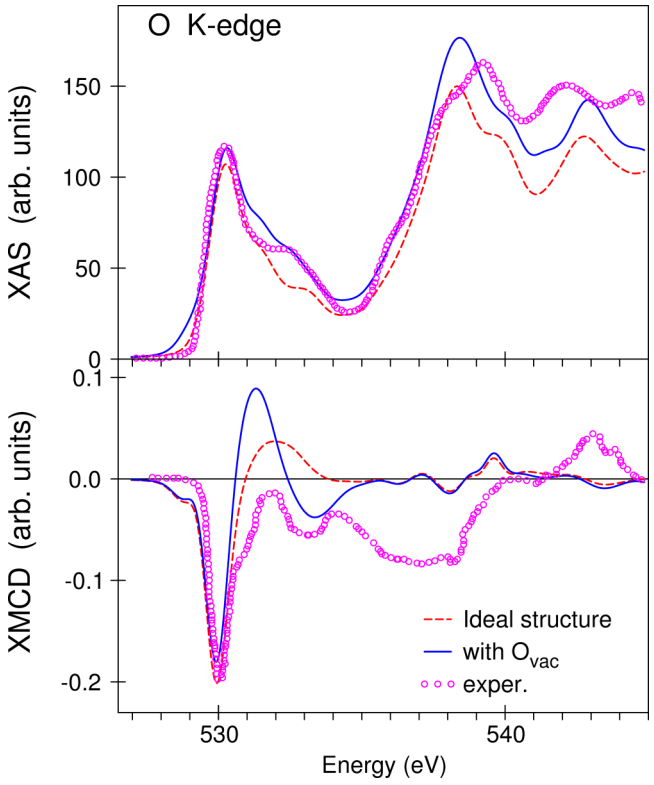

FIG. 5. Comparison between the experimental [43] (circles) x-ray absorption (upper panel) and x-ray magnetic circular dichroism (lower panel) at the O K edges of $BaFeO_3$ and the spectra calculated by the LMTO method in the GGA + U approximation ($U_{\text{eff}} = 3$ eV) (black solid lines). The red dashed line shows the spectra for the ideal crystal structure, while the dotted blue line presents the theoretical spectra with an oxygen vacancy.

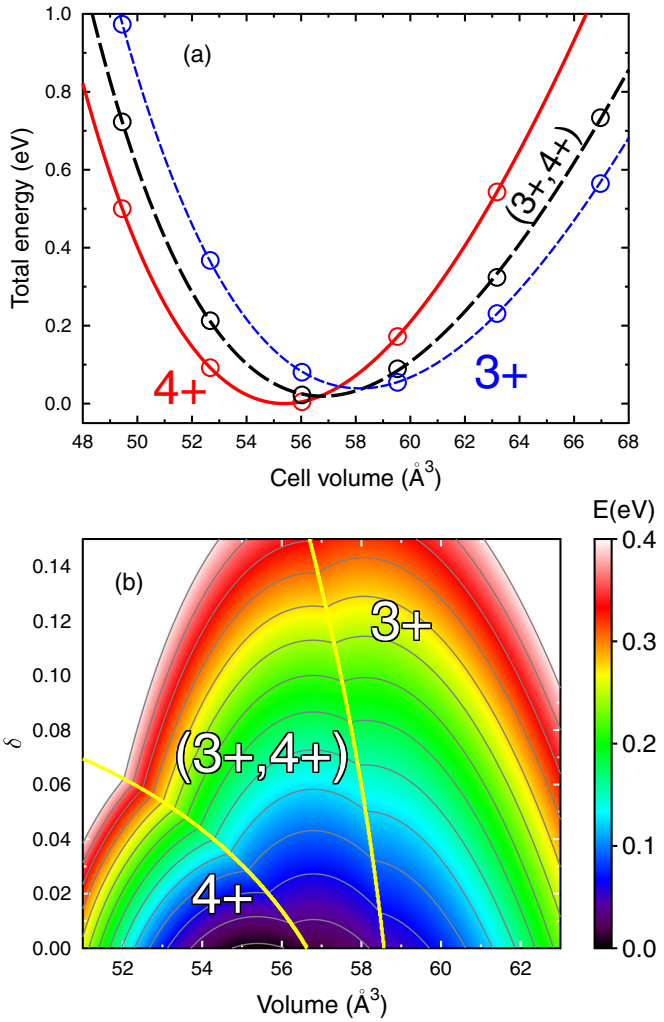

FIG. 6. The total and formation energies of $BaFeO_{3-\delta}$, calculated using the LSDA-SIC method for the Fe^{4+}, Fe^{3+}, and a combination of them: (a) Total energies as functions of the volume without oxygen vacancies; (b) formation energy as a function of volume and δ.

interaction Fe-O-Fe can be switched from antiferromagnetic to ferromagnetic when the Fe 3d orbital filling changes. In this context, a variety of superexchange options, such as Fe^{4+}-O-Fe^{4+}, Fe^{3+}-O-Fe^{3+}, and Fe^{4+}-O-Fe^{3+}, need to be inspected. However, the Goodenough-Kanamori simplifications work robustly for insulators only. When theory deals with a metallic and magnetic oxide, such as cubic BFO, the superexchange coupling does not dominate and the double exchange complicates the long-range interactions between magnetic species.

In the case of cubic symmetry, the Fe^{4+} electronic configuration is $t_{2g}^3 e_g^1$, where the half-occupied e_g orbital has either a $d_{3z^2-r^2}$ or a $d_{x^2-y^2}$ representation. For the cubic BFO case, which was treated within the LSDA-SIC model, we found that the two e_g options result in the same equilibrium volume (see Fig. 6), which is substantially smaller than the experimental result (62.57 Å^3) and the volume calculated using the GGA (Fe^{2+}). Although the volume computed within the GGA is very close to the experimental value, the corresponding total energy is about 22 meV higher than the total energies of the Fe^{4+} and Fe^{3+} configurations.

For the cation Fe^{3+}, its t_{2g} and e_g levels must be fully occupied in the majority spin channel. This electronic configuration yields the total-energy minimum value, which is not far above that of the Fe^{4+} ground state, as shown in Fig. 6(a). The calculated equilibrium volume is in better agreement with the experimental results than the values obtained for Fe^{3+} (SIC) and Fe^{2+} (GGA) configurations. The energetics suggest that both oxidations, Fe^{4+} and Fe^{3+}, can be realized in epitaxially fabricated thin films. Configurations with other oxidation states are much higher in energy and are excluded from further consideration.

Further, we compared the formation energies of Fe^{4+} and Fe^{3+} oxidation states in the presence of oxygen vacancies. The formation energy was calculated using the following simplified formula:

$$E_f = E_{BaFeO_{3-\delta}} - E_{Ba} - E_{Fe} - (3-\delta)E_O, \qquad (3)$$

where $E_{BaFeO_{3-\delta}}$ is the total energy of BFO in the presence of oxygen vacancies, and E_{Ba}, E_{Fe}, and E_O are the total energies of free atoms, calculated in the same density-functional approximation used in the BFO case.

For $\delta = 0.03$, the total energies in the equilibrium volumes are almost the same (see Fig. 6). Thus, the vacancy formation lowers the energy of the Fe^{3+} oxidation state, which agrees

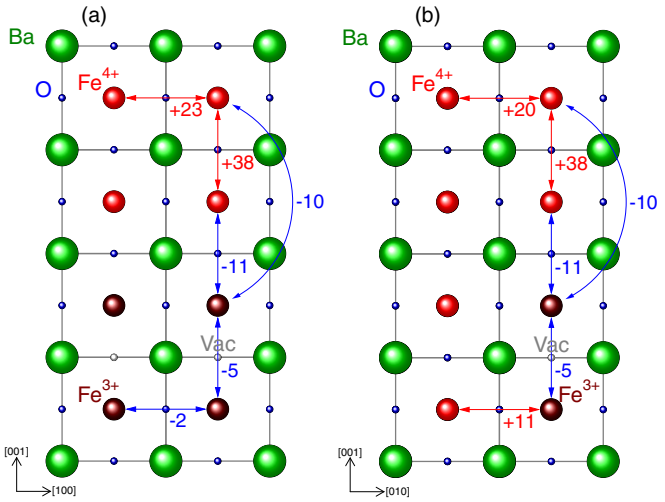

FIG. 7. Exchange interaction coefficients (in meV) of $BaFeO_{2.875}$, which were calculated using the $2 \times 2 \times 4$ supercell, are shown for the planes (010) and (100) in panels (a) and (b), respectively.

with our interpretation of the XAS and XMCD experiments. In a real BFO sample, both oxidation states can coexist, which is also evident from our XAS and XMCD simulations. In Fig. 6 we present the total energy for a mixed configuration, which is lower than the others in a particular concentration range.

As a next step, we investigated the impact of oxygen vacancies on the magnetic properties of the BFO. The oxygen vacancies were simulated within a $2 \times 2 \times 4$ supercell, in which one oxygen site was occupied by a vacancy with a given probability. Here we used the same supercell approximation applied for our XAS and XMCD simulations. The use of the supercell enables us to take into account short-range effects in a simple manner, which can take place in real materials. Results for the exchange interaction, computed in this supercell and $\delta = 0.25$, are presented in Fig. 7. While the exchange interaction between the Fe^{4+} cations is strong and positive, it is week and negative between the Fe^{3+} atoms.

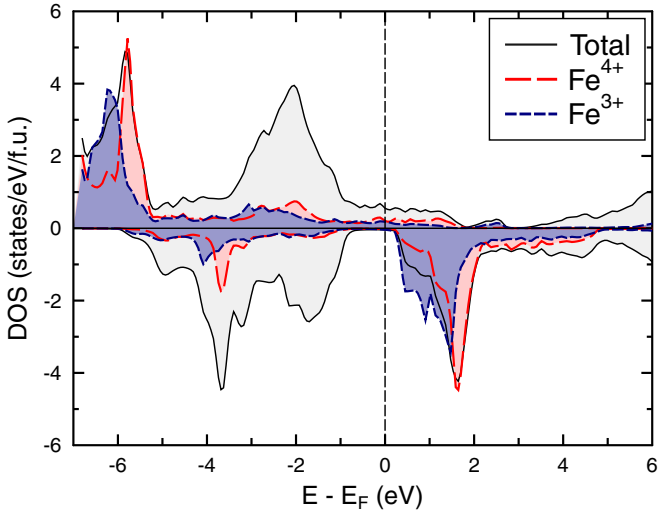

FIG. 8. DOS of the $BaFeO_{2.875}$ simulated in a $2 \times 2 \times 4$ supercell.

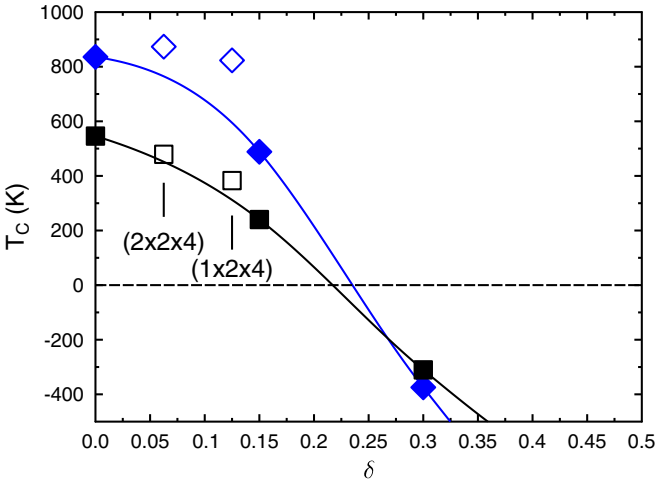

FIG. 9. Critical temperature T_C in $BaFeO_{3-\delta}$ as a function of oxygen vacancy concentration δ: blue and black lines show T_C in the mean-field and random-phase approximations, respectively. Open figures, supercell approach; filled, CPA. Here, the negative T_C means the absence of ferromagnetic order.

The reason for this can be understood from the DOS, shown in Fig. 8. Because of the vacancy (missing oxygen), the $3d$ states of the Fe^{3+} are more localized (in particular the e_g states) and are shifted down in energy. This increases the tendency to an antiferromagnetic coupling. The coupling between the atoms in different oxidation states is also antiferromagnetic and very strong due to the large difference in the DOS. This finding agrees with the main conclusions of Mori, who first developed a model for the magnetic structure of $BaFeO_x$ [44].

Depending on the vacancy concentration and their distribution, the nontrivial exchange interaction in $BaFeO_{3-\delta}$ can result in various magnetic orders. In Fig. 9, we show the change of critical temperature with the oxygen vacancy concentration simulated within the MFA and RPA approaches. The calculations were performed within both the CPA and supercell approaches. The negative T_C means here the absence of ferromagnetic order (either antiferromagnetic or noncollinear). First of all, the CPA and supercell calculations agree very well with each other. For comparison, we used two different supercells—$2 \times 2 \times 4$ and $1 \times 2 \times 4$—to simulate the vacancy concentrations of $\delta = 0.0625$ and 0.125, respectively. Thus, for a moderate vacancy concentration δ of 0.15–0.20, T_C lies in the experimental range of 250–100 K.

IV. SUMMARY

In this work, we studied the electronic and magnetic properties of cubic $BaFeO_3$ within a DFT framework using GGA and GGA + U approaches. We predicted that $BaFeO_3$ in an ideal stoichiometric cubic structure should be half-metallic and ferromagnetic with a high Curie temperature of 700–900 K. However, this finding disagrees with experiments, which found that the compound has a T_C far below room temperature. To understand this discrepancy, we simulated XAS and XMCD spectra comparing the theoretically obtained results with available experimental data. In this model, we varied the chemical composition and the structural and electronic parameters to

obtain a better agreement with experiments. Our simulations showed that the experimental observations can be explained by oxygen vacancies, which can be present in real BFO samples. Thereby, Fe atoms near an oxygen vacancy change their oxidation state from 4+ to 3+. Thus, a real cubic $BaFeO_3$ may contain both Fe^{4+} and Fe^{3+} cations, which explains the experimentally observed double-peak structure in XAS and XMCD spectra. Further, here we found that oxygen vacancies can substantially reduce the Curie temperature of a cubic BFO or even change the ferromagnetic order to an antiferromagnetic one or a noncollinear structure. The reason for this is a strong antiferromagnetic exchange coupling between Fe atoms of different oxidation states. This result provides a clear route to fabricate robust ferromagnetic $BaFeO_3$ with a high Curie temperature by reducing the amount of oxygen vacancies and stabilizing it in the cubic structure.

ACKNOWLEDGMENTS

This work is supported by the DFG within the Collaborative Research Center *Sonderforschungsbereich* SFB 762, "Functionality of Oxide Interfaces."

[1] V. Garcia, M. Bibes, L. Bocher, S. Valencia, F. Kronast, A. Crassous, X. Moya, S. Enouz-Vedrenne, A. Gloter, D. Imhoff *et al.*, Science **327**, 1106 (2010).
[2] S. Valencia, A. Crassous, L. Bocher, V. Garcia, X. Moya, R. Cherifi, C. Deranlot, K. Bouzehouane, S. Fusil, A. Zobelli *et al.*, Nat. Mater. **10**, 753 (2011).
[3] H. L. Meyerheim, F. Klimenta, A. Ernst, K. Mohseni, S. Ostanin, M. Fechner, S. Parihar, I. V. Maznichenko, I. Mertig, and J. Kirschner, Phys. Rev. Lett. **106**, 087203 (2011).
[4] L. Martin and R. Ramesh, Acta Mater. **60**, 2449 (2012).
[5] D. Pantel, S. Goetze, D. Hesse, and M. Alexe, Nat. Mater. **11**, 289 (2012).
[6] S. Chakraverty, T. Matsuda, N. Ogawa, H. Wadati, E. Ikenaga, M. Kawasaki, Y. Tokura, and H. Hwang, Appl. Phys. Lett. **103**, 142416 (2013).
[7] N. Hayashi, T. Yamamoto, H. Kageyama, M. Nishi, Y. Watanabe, T. Kawakami, Y. Matsushita, A. Fujimori, and M. Takano, Angew. Chem. **123**, 12755 (2011).
[8] B. Ribeiro, R. Borges, R. da Silva, N. Franco, P. Ferreira, E. Alves, B. Berini, A. Fouchet, N. Keller, and M. Godinho, J. Appl. Phys. **111**, 113923 (2012).
[9] C. Callender, D. P. Norton, R. Das, A. Hebard, and J. D. Budai, Appl. Phys. Lett. **92**, 012514 (2008).
[10] H. A. Jahn and E. Teller, Proc. R. Soc. London, Ser. A **161**, 220 (1937).
[11] J. Rodríguez-Carvajal, M. Hennion, F. Moussa, A. H. Moudden, L. Pinsard, and A. Revcolevschi, Phys. Rev. B **57**, R3189(R) (1998).
[12] Q. Huang, A. Santoro, J. W. Lynn, R. W. Erwin, J. A. Borchers, J. L. Peng, K. Ghosh, and R. L. Greene, Phys. Rev. B **58**, 2684 (1998).
[13] J. Hemberger, A. Krimmel, T. Kurz, H.-A. Krug von Nidda, V. Y. Ivanov, A. A. Mukhin, A. M. Balbashov, and A. Loidl, Phys. Rev. B **66**, 094410 (2002).
[14] N. Hayashi, T. Yamamoto, A. Kitada, A. Matsuo, K. Kindo, J. Hester, H. Kageyama, and M. Takano, J. Phys. Soc. Jpn. **82**, 113702 (2013).
[15] D. Fuks, Y. Mastrikov, E. Kotomin, and J. Maier, J. Mater. Chem. A **1**, 14320 (2013).
[16] T. Li, Z. Feng, C. Jing, F. Hong, S. Cao, and J. Zhang, Eur. Phys. J. B **86**, 414 (2013).
[17] B. Ribeiro, M. Godinho, C. Cardoso, R. Borges, and T. Gasche, J. Appl. Phys. **113**, 083906 (2013).
[18] M. Mostovoy, Phys. Rev. Lett. **94**, 137205 (2005).
[19] Z. Li, R. Laskowski, T. Iitaka, and T. Tohyama, Phys. Rev. B **85**, 134419 (2012).
[20] Z. Li, T. Iitaka, and T. Tohyama, Phys. Rev. B **86**, 094422 (2012).
[21] M. Lüders, A. Ernst, M. Däne, Z. Szotek, A. Svane, D. Ködderitzsch, W. Hergert, B. L. Györffy, and W. M. Temmerman, Phys. Rev. B **71**, 205109 (2005).
[22] M. Geilhufe, S. Achilles, M. A. Köbis, M. Arnold, I. Mertig, M. Hergert, and A. Ernst, J. Phys. Condens. Matter **27**, 435202 (2015).
[23] J. P. Perdew, K. Burke, and M. Ernzerhof, Phys. Rev. Lett. **77**, 3865 (1996).
[24] J. P. Perdew and A. Zunger, Phys. Rev. B **23**, 5048 (1981).
[25] V. I. Anisimov, J. Zaanen, and O. K. Andersen, Phys. Rev. B **44**, 943 (1991).
[26] A. I. Liechtenstein, M. I. Katsnelson, V. P. Antropov, and V. A. Gubanov, J. Magn. Magn. Mater. **67**, 65 (1987).
[27] S. Tyablikov, *Methods in the Quantum Theory of Magnetism* (Springer Science+Business Media, New York, 1967).
[28] G. Fischer, M. Däne, A. Ernst, P. Bruno, M. Lüeders, Z. Szotek, W. Temmerman, and W. Hergert, Phys. Rev. B **80**, 014408 (2009).
[29] C. Etz, I. V. Maznichenko, D. Böttcher, J. Henk, A. N. Yaresko, W. Hergert, I. I. Mazin, I. Mertig, and A. Ernst, Phys. Rev. B **86**, 064441 (2012).
[30] B. L. Gyorffy, Phys. Rev. B **5**, 2382 (1972).
[31] T. Oguchi, K. Terakura, and N. Hamada, J. Phys. F **13**, 145 (1983).
[32] B. L. Gyorffy, A. J. Pindor, J. Staunton, G. M. Stocks, and H. Winter, J. Phys. F **15**, 1337 (1985).
[33] O. K. Andersen, Phys. Rev. B **12**, 3060 (1975).
[34] V. V. Nemoshkalenko, A. E. Krasovskii, V. N. Antonov, Vl. N. Antonov, U. Fleck, H. Wonn, and P. Ziesche, Physica Status Solidi (b) **120**, 283 (1983).
[35] V. N. Antonov, H. A. Dür, Y. Kucherenko, L. V. Bekenov, and A. N. Yaresko, Phys. Rev. B **72**, 054441 (2005).
[36] V. N. Antonov, O. Jepsen, A. N. Yaresko, and A. P. Shpak, J. Appl. Phys. **100**, 043711 (2006).
[37] V. N. Antonov, A. N. Yaresko, and O. Jepsen, Phys. Rev. B **81**, 075209 (2010).
[38] G. Kresse and J. Furthmüller, Phys. Rev. B **54**, 11169 (1996).

[39] X. D. Zou, S. Hovmöller, M. Parras, J. M. González-Calbet, M. Vallet-Regí, and J. C. Grenier, Acta Crystallogr. Sect. A **49**, 27 (1993).
[40] M. Pajda, J. Kudrnovský, I. Turek, V. Drchal, and P. Bruno, Phys. Rev. B **64**, 174402 (2001).
[41] V. I. Anisimov, F. Aryasetiawan, and A. I. Lichtenstein, J. Phys. Condens. Matter **9**, 767 (1997).
[42] V. N. Antonov, B. N. Harmon, A. N. Yaresko, and A. P. Shpak, Phys. Rev. B **75**, 184422 (2007).
[43] T. Tsuyama, T. Matsuda, S. Chakraverty, J. Okamoto, E. Ikenaga, A. Tanaka, T. Mizokawa, H. Y. Hwang, Y. Tokura, and H. Wadati, Phys. Rev. B **91**, 115101 (2015).
[44] S. Mori, J. Phys. Soc. Jpn. **28**, 44 (1970).